ELSEVIER

Volume 183, Issue 9, September 2010

JOURNAL OF SOLID STATE CHEMISTRY

www.elsevier.com/locate/jssc

CONTENTS

Abstracted/indexed in BioEngineering Abstracts, Chemical Abstracts, Coal Abstracts, Current Contents/Physics, Chemical, & Earth Sciences, Engineering Index, Research Alert, SCISEARCH, Science Abstracts, and Science Citation Index. Also covered in the abstract and citation database SCOPUS®. Full text available on ScienceDirect®.

Regular Articles

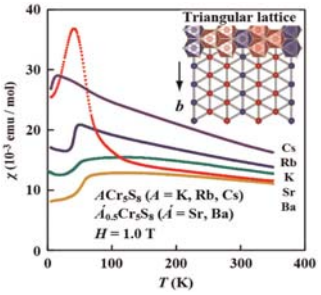

Temperature dependences of magnetic susceptibilities for pseudo-hollandite sulfides, ACr_5S_8 (A = K, Rb, Cs) and $A_{0.5}'Cr_5S_8$ (A' = Sr, Ba). The observed magnetic frustration effect originates in the triangular lattice.

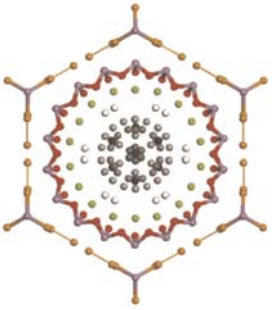

The novel crystalline microporous semiconductor Rb-CTH-1 shows heat-induced reversible sorption of disordered guest species and desorption-induced irreversible rearrangements of ordered guest ions with a response in its semiconductive properties.

Regular Articles—Continued

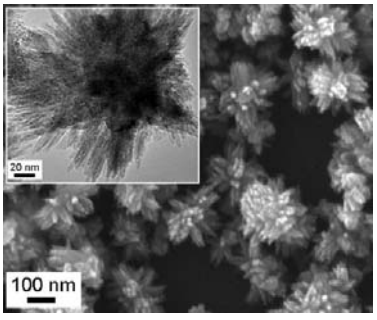

Flower-like TiO_2 nanostructures synthesized by a nonaqueous seeded growth without using any structural directing or capping agents.

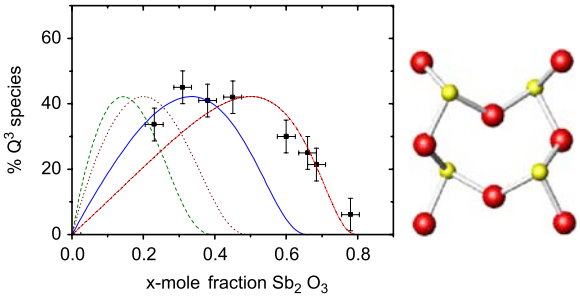

Antimony silicate glasses have been shown to contain Sb^{3+} in [:SbO_3] trigonal pyramid units using ^{121}Sb Mössbauer spectroscopy and Raman spectroscopy. ^{29}Si magic-angle-spinning NMR has shown silicon Q^n speciation which can be interpreted as formation of rings of 4 [:SbO_3] units such as are found in valentinite.

Continued

Crystal growth and properties of $Ln_2Ag_{1-x}Ga_{10-y}$ (Ln = La, Ce), a disordered variant of the Ce_2NiGa_{10}-structure type
Melissa C. Menard, Yimin Xiong, Amar B. Karki, Brenton L. Drake, Philip W. Adams, Frank R. Fronczek, David P. Young and Julia Y. Chan
Page 1935

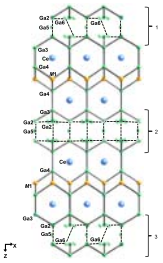

The figure illustrates the structure of $Ce_2Ag_{0.7(1)}Ga_{9.1(1)}$, which can be described as a distorted variant of the Ce_2NiGa_{10} structure. The distorted gallium segments are best described as variants of $CeGa_6$ ($PuGa_6$-structure type), and the distorted Ce(Ag,Ga)$_4$-type segments are built of layers of face-sharing tetragonal antiprisms. Here M = Ag + Ga and the shaded atoms are partially occupied.

Synthesis, crystal structure and thermal behavior of two hydrated forms of lanthanide phthalates $Ln_2(O_2 + C_6H_4–CO_2)_3(H_2O)$ (Ln = Ce, Nd) and $Nd_2(O_2C–C_6H_4–CO_2)_3(H_2O)_3$
David Pizon, Natacha Henry, Thierry Loiseau, Pascal Roussel and Francis Abraham
Page 1943

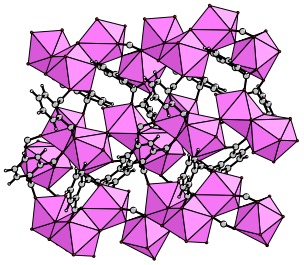

New members of the chain-like structures of neodymium phthalates with different hydration states $Nd_2(1,2\text{-bdc})_3(H_2O)_x$ (x = 1 or 2, 1–2bdc = phthalate group) and comparison with cerium-based analogs.

New divalent manganese complex with pyridine carboxylate N-oxide ligand: Synthesis, structure and magnetic properties
Fu-Chen Liu, Min Xue, Hai-Chao Wang and Jie Ou-Yang
Page 1949

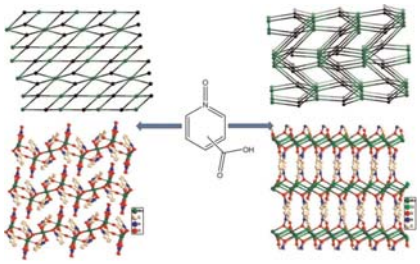

The synthesis, crystal structure and magnetic properties of two new MnII complexes with pyridyl-carboxylate N-oxide ligands are reported.

Syntheses, crystal structures, and properties of three new metal selenites $Na_2Co_2(SeO_3)_3$, $Na_2Co_{1.67}Ni_{0.33}(SeO_3)_3$, and $Na_2Ni_2(SeO_3)_3$
Xiao-Qing Yuan, Mei-Ling Feng, Jian-Rong Li and Xiao-Ying Huang
Page 1955

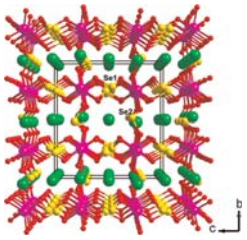

Three new isostructural metal selenites, $Na_2Co_2(SeO_3)_3$, $Na_2Co_{1.67}Ni_{0.33}(SeO_3)_3$, and $Na_2Ni_2(SeO_3)_3$ have been hydro-/solvothermally synthesized and characterized. Their structures feature three-dimensional open frameworks with Na^+-occupied channels.

Magnetic and electrical properties of quadruple perovskites with 12 layer structures $Ba_4LnM_3O_{12}$ (Ln = rare earths; M = Ru, Ir): The role of metal–metal bonding in perovskite-related oxides
Yuki Shimoda, Yoshihiro Doi, Makoto Wakeshima and Yukio Hinatsu
Page 1962

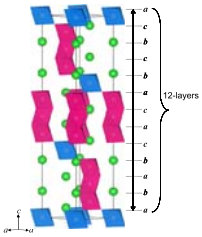

Structures and magnetic and electrical properties of quadruple perovskites containing rare earths $Ba_4LnM_3O_{12}$ (Ln = rare earths; M = Ru, Ir) were investigated. They crystallize in the 12L-perovskite-type structure. All the $Ba_4Ln^{3+}Ru_3^{4.33+}O_{12}$ compounds show magnetic ordering at low temperatures, while any of the corresponding iridium-containing compounds $Ba_4Ln^{3+}Ir_3^{4.33+}O_{12}$ is paramagnetic down to 1.8 K. $Ba_4Ce^{4+}Ir_3^{4+}O_{12}$ orders antiferromagnetically at 10.5 K, while the corresponding ruthenium-containing compound $Ba_4Ce^{4+}Ru_3^{4+}O_{12}$ is paramagnetic. These magnetic results were well understood by the magnetic behavior of M_3O_{12}. The electrical resistivity measurements show that these compounds demonstrate two-dimensional Mott-variable range hopping behavior.

A new structure type of $RE_4B_4O_{11}F_2$: High-pressure synthesis and crystal structure of $La_4B_4O_{11}F_2$
Almut Haberer, Reinhard Kaindl, Oliver Oeckler and Hubert Huppertz
Page 1970

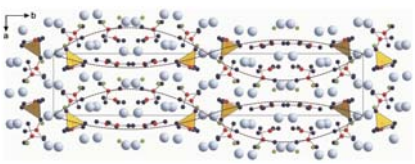

A new structure type of $RE_4B_4O_{11}F_2$: high-pressure synthesis and crystal structure of $La_4B_4O_{11}F_2$.

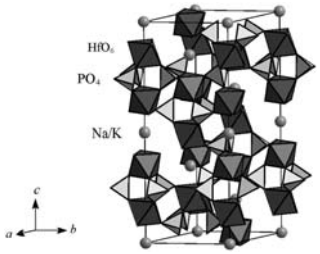

The incorporation possibilities of different alkali elements into crystalline phosphates $A_{1-x}A'_xHf_2(PO_4)_3$ (A = Li, Na, K, Rb, Cs) were studied, the formation regions of kosnarite solid solutions were determined. $Na_{0.5}K_{0.5}Hf_2(PO_4)_3$ crystal structure was studied by powder X-ray diffraction, and the distribution of alkali metals in kosnarite structure was found out. The phosphate crystallizes in the space group $R\bar{3}c$, with $a = 8.7295(1)$ Å, $c = 23.2023(4)$ Å, $V = 1531.24(4)$ Å^3, $Z = 6$; $R_{wp} = 6.15$, $R_p = 4.43$. The concentration region knowledge of the kosnarite phase existence and peculiarities of their phase formation in the $A_{1-x}A'_xM_2(PO_4)_3$ (M = Ti, Zr, Hf) systems allow us to choose phosphate matrice compositions suitable for solidification of reprocessing wastes of spent U–Pu nuclear fuels.

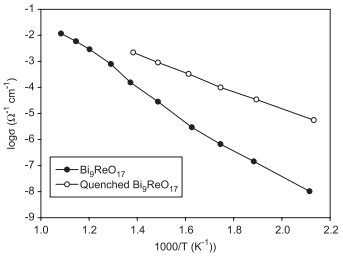

The structure of Bi_9ReO_{17} is discussed and related to the ionic conductivity of the ordered and disordered forms.

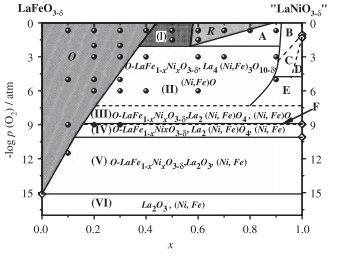

Isothermal $LaFeO_{3-\delta}$–"$LaNiO_{3-\delta}$" section of the phase diagram of the La–Fe–Ni–O system at 1100 °C. The hatched areas represent single phase regions: O-$LaFe_{1-x}Ni_xO_{3-\delta}$ ($x \le 0.4$) with orthorhombically distorted perovskite structure and R-$LaFe_{1-x}Ni_xO_{3-\delta}$ ($0.6 \le x < 0.8$) with rhombohedral one.

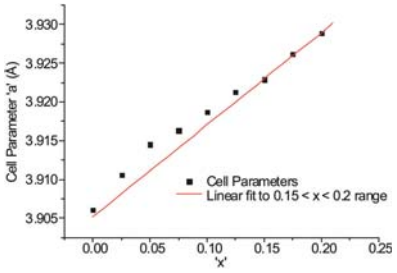

Change in cell dimensions for the series $Sr_{1-x}Ti_{1-2x}Nb_{2x}O_3$, $0 \le x \le 0.2$.

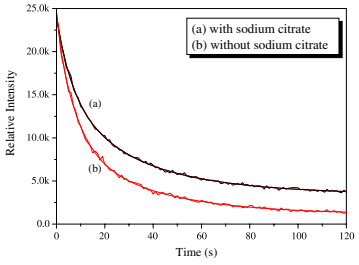

We present a simple and efficient hydrothermal treatment and subsequently postannealing approach to prepare $Sr_3Al_2O_6$: Eu^{2+} (Eu^{3+}), Dy^{3+} phosphors on a large scale.

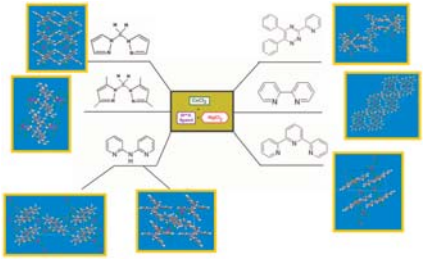

N–N: bis(3,5dimethylpyrazol-1-yl)methane (bdmpzm), 2,2-dipyridylamine (dpa), 5,6-diphenyl-3-(2-pyridyl)-1,2,4-trazine (dppt) and 2,2′-bipyridine (bipy), 6′,2″-terpyridine (terpy).

Continued

Synthesis and characterization of Pd(0), PdS, and Pd@PdO core–shell nanoparticles by solventless thermolysis of a Pd–thiolate cluster
Deepa Jose and Balaji R. Jagirdar
Page 2059

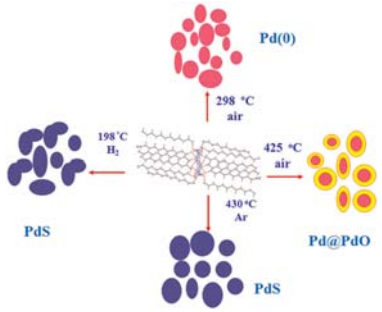

Solventless thermolysis of a single palladium–thiolate cluster affords various Pd systems such as Pd(0), Pd@PdO core–shell, and PdS nanoparticles demonstrating the versatility of the precursor and the methodology.

Second order incommensurate phase transition in 25L-Ta_2O_5
M. Audier, B. Chenevier, H. Roussel and A. Lintanf Salaün
Page 2068

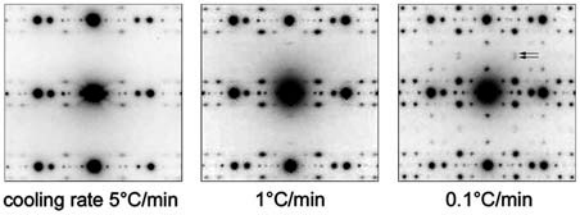

Electron diffraction patterns of [100] zone axis, showing a structural change of the 25L-Ta_2O_5 phase through a variation of the cooling rate from 1000 °C.

The new binary intermetallic $YbGe_{2.83}$
C. Peter Sebastian and Mercouri G. Kanatzidis
Page 2077

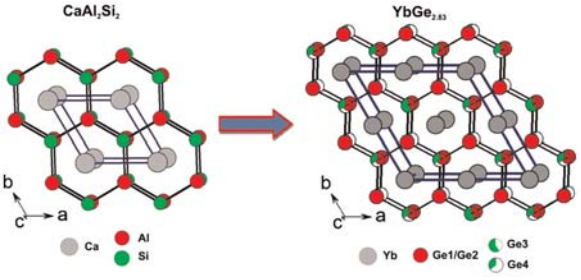

The new binary compound $YbGe_{2.83}$ is a variant of the $CaAl_2Si_2$ structure type with ordered vacancies. Zintl formalism and valence bond sum calculations suggest intermediate valence of Yb ions in $YbGe_{2.83}$.

Polymorphism of new rubidium magnesium monophosphate
Rajia Ait Benhamou, Gilles Wallez, Pascal Loiseau, Bruno Viana, Mohamed Elaatmani, Mohamed Daoud and Abdelwahed Zegzouti
Page 2082

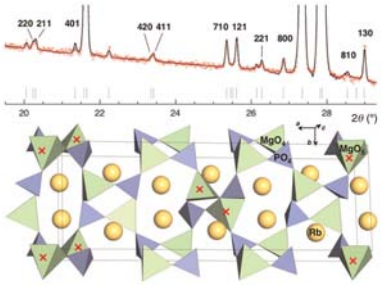

Superstructure $h\,k\,l$, $h \neq 3n$ diffraction peaks of low-temperature $RbMgPO_4$ results of the transformation of 1/3 of the MgO_4 tetrahedra into MgO_5 pyramids.

Syntheses, crystal structures and vibrational spectra of $KLn(SO_4)_2 \cdot H_2O$ (Ln = La, Nd, Sm, Eu, Gd, Dy)
Karolina Kazmierczak and Henning A. Höppe
Page 2087

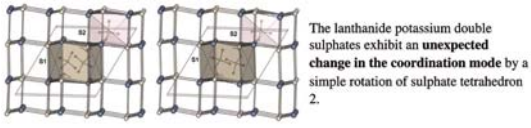

The lanthanide potassium double sulphates exhibit an unexpected change in the coordination mode by a simple rotation of sulphate tetrahedron 2.

Symmetry of $LaAlO_3$ nanocrystals as a function of crystallite size
P.J. Dereń, K. Lemański, A. Gągor, A. Watras, M. Małecka and M. Zawadzki
Page 2095

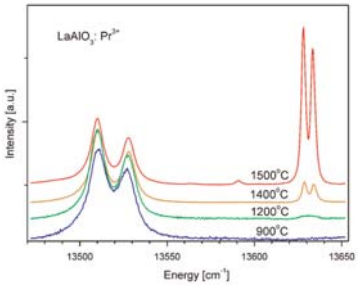

The 77 K emission spectra of $LaAlO_3:Pr^{3+}$ nanocrystallites codoped with Cr^{3+} as a function of the annealing temperature. Intensities were normalized to the maximum of the $^3P_0 \rightarrow {}^3H_4$ transition. The R line at 13633 cm^{-1} vanish with decreasing the nanocrystals size and is absent for the smallest ones.

Continued

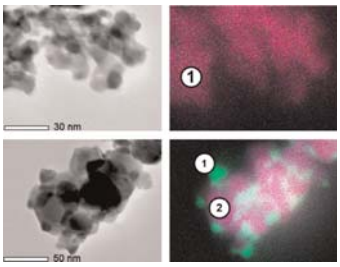

Sn-doped or Sn/Mg-doped Fe_2O_3 hematites, were analyzed by X-ray diffraction refinement, Mössbauer spectroscopy, magnetic characterization and TEM investigations. Their color is correlated to the doping ions concentration.

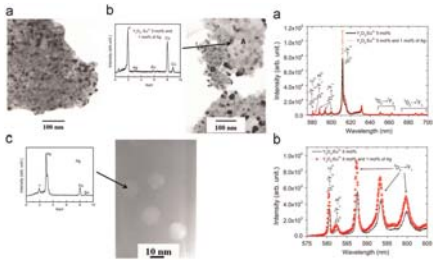

The presence of Ag nanoparticles together $Y_2O_3:Eu^{3+}$ 5 mol% phosphor showed to affect directly the optical and crystallinity of the material. Luminescence spectra show directly the effect observed.

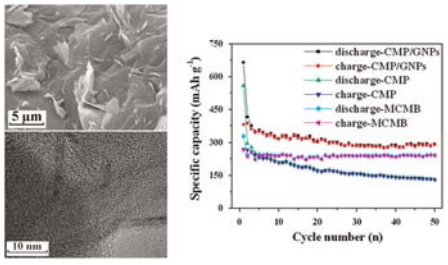

Uniform mesophase pitch/exfoliated graphite nanoplatelets nanocomposite has been efficiently fabricated with an initiation of graphite intercalation compounds. The as-prepared composite electrode exhibited high electrochemical performance for Li-ion batteries.

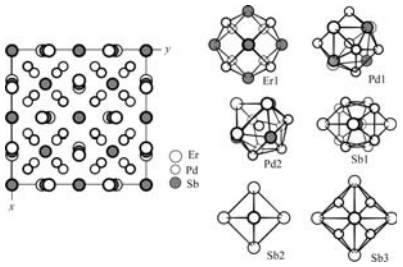

Projection of the crystal structure of $Er_3Pd_8Sb_4$ onto XY plane and the coordination polyhedra of all the atoms.

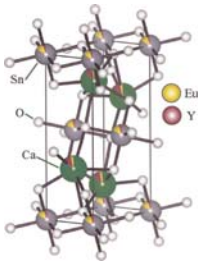

The composition of $Ca_{1.8}Eu_{0.2}Y_{0.2}Sn_{0.8}O_4$ determined by electron channeling microanalysis is graphically shown, where the rare-earth dopants, Eu and Y preferentially occupy the Ca and Sn sites, respectively, to maintain the local charge neutrality.

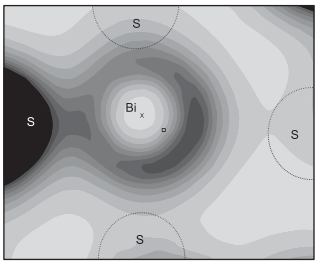

The article includes charge density maps used to analyze the charge distribution around bismuth in sulfides. This map shows the orientation of a lone electron pair.

Metal coordination architectures of N-propionyl-1-hydroxy-2-naphthoylhydrazide: From metalladiazamacrocycles to trinuclear complexes

Xuefeng Shi, Dacheng Li, Suna Wang, Suyuan Zeng, Daqi Wang and Jianmin Dou

Page 2144

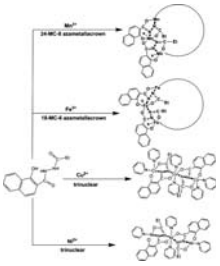

One 24-membered octanuclear and one 18-membered hexanuclear metalladiazamacrocycles as well as two linear trinuclear complexes have been reported from a trianionic pentadentate bridging ligand N-propionyl-1-hydroxy-2-naphthoylhydrazide (H_3pnhz).

A nitrilo-tri-acetic-acid/acetic acid route for the deposition of epitaxial cerium oxide films as high temperature superconductor buffer layers

T.T. Thuy, P. Lommens, V. Narayanan, N. Van de Velde, K. De Buysser, G.G. Herman, V. Cloet and I. Van Driessche

Page 2154

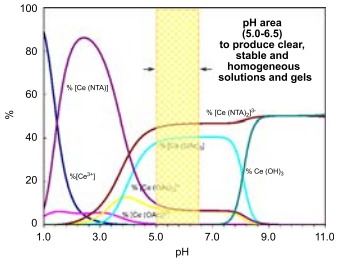

Study of the complexation and hydrolysis behavior of Ce^{4+} ions in the presence of nitrilo-tri-acetic acid and the subsequent development of an aqueous chemical solution deposition route suited for the processing of textured CeO_2 buffer layers on Ni–W tapes.

Synthesis and luminescence properties of Yb^{3+} and Er^{3+} doped $KLa(WO_4)_2$ nanoparticles

Meng Chen, Tongqing Sun, Hong Chen, Yu Zhang, Li Wu, Yongfa Kong and Jingjun Xu

Page 2161

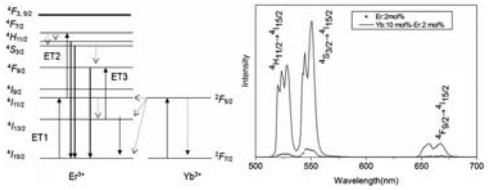

Er^{3+} and Yb^{3+} codoped $KLa(WO_4)_2$ nanoparticles have been prepared by Pechini method. Luminescence studies showed that the intensity of upconversion emission of the Yb^{3+} and Er^{3+} codoped samples was much stronger than that of the Er^{3+} single doped samples (pumped by 980 nm LD), and the upconversion emission mechanisms suggested that all the three bands of upconversion emissions were two-photon process.

Ethanol-assisted hydrothermal synthesis and electrochemical properties of coral-like β-$Co(OH)_2$ nanostructures

Shaochun Tang, Sascha Vongehr, Yang Wang, Lan Chen and Xiangkang Meng

Page 2166

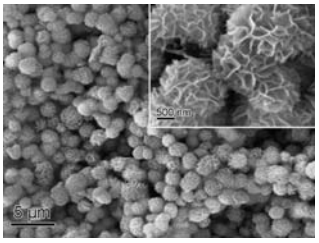

Coral-like β-$Co(OH)_2$ nanostructures were synthesized via a facile ethanol-assisted hydrothermal route. Their high porosity facilitates a deep penetration by electrolytes and thus contributes to the excellent capacitive properties.

Syntheses, structures and properties of silver(I) complexes with flexible 1,3,5-tris(pyridylmethoxyl)benzene ligands

Gang Wu, Xiao-Feng Wang, Taka-aki Okamura, Min Chen, Wei-Yin Sun and Norikazu Ueyama

Page 2174

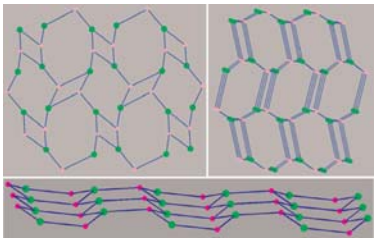

Five new silver(I) coordination frameworks with different topology were obtained and their structures were determined by single crystal X-ray diffraction studies. The influence of counteranion and ligand on the structure of complexes was discussed, the photoluminescence and anion-exchange properties were reported.

Synthesis and structural characterization of $Al_4Si_2C_5$-homeotypic aluminum silicon oxycarbide, $(Al_{6-x}Si_x)(O_yC_{5-y})$ ($x \sim 0.8$ and $y \sim 1.6$)

Motoaki Kaga, Daisuke Urushihara, Tomoyuki Iwata, Keita Sugiura, Hiromi Nakano and Koichiro Fukuda

Page 2183

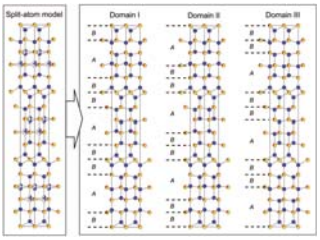

A new aluminum silicon oxycarbide, $(Al_{6-x}Si_x)(O_yC_{5-y})$ ($x \sim 0.8$ and $y \sim 1.6$). The crystal is composed of three types of domains (I, II and III), and hence the structure is represented by a split-atom model. Individual crystal structures can be regarded as layered structures, which consist of *A*-type $[(Al,Si)_4(O,C)_4]$ unit layers and *B*-type $[(Al,Si)(O,C)_2]$ single layers.

Continued

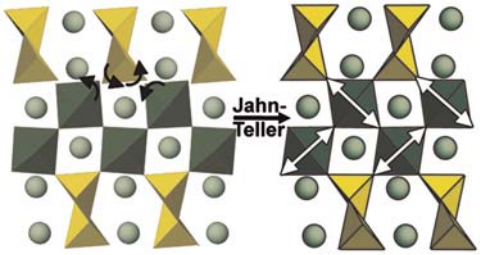

Order of the Jahn–Teller distorted MnO_6 octahedra in $Pb_2Mn_2O_5$. Two long and two short bonds lie in the *a*–*c* plane, along two perpendicular orientations within this plane, forming a *d*-type pattern.

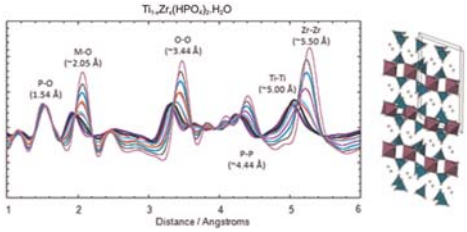

Layered phosphates of general formula $(Ti_{1-x}Zr_x)(HPO_4) \cdot H_2O$ have been prepared by the hydrothermal treatment of amorphous gels in phosphoric acid and characterised by Rietveld analysis of high resolution synchrotron X-ray powder diffraction data and pair distribution function analysis of high energy synchrotron X-ray total scattering data.

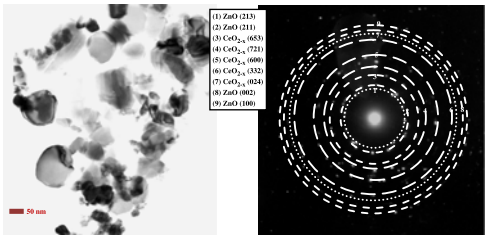

TEM micrographs and their corresponding SAED pattern obtained for the as-deposited ZnO–CeO_{2-x} thin films for a Zn/Ce metallic ratio 16:9.

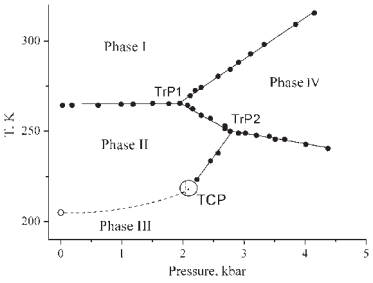

p–*T* phase diagram of $(NH_4)_3TiOF_5$.

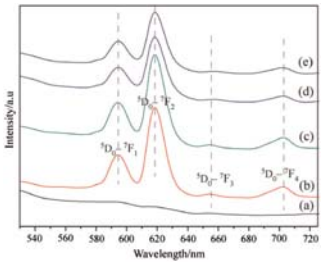

A series of Mg–Al–Eu ternary hydrotalcite-like layered double hydroxides (LDHs), with Mg/(Al + Eu) atomic ratios ranging from 1.3/1, 2/1 3/1 to 4/1, were synthesized by a coprecipitation method. The photoluminescent spectra of the Mg–Al–Eu ternary LDHs are described by the well-known $^5D_0$–^7F_J transition ($J = 1, 2, 3, 4$) of Eu^{3+} ions with the strongest emission for $J = 2$.

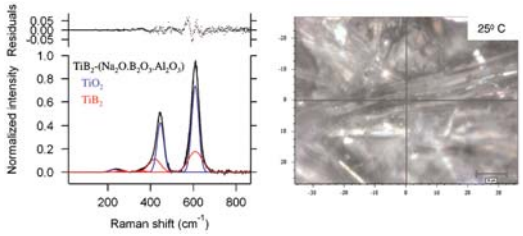

Deconvolution of the reduced Raman spectrum of the grain phase in TiB_2–($Na_2O \cdot B_2O_3 \cdot Al_2O_3$) composite along with its Raman micrographs collected at room temperature.

Humidity effects in $Fe_{16}N_2$ fine powder preparation by low-temperature nitridation

Kohetsu Yamanaka, Yuki Onuma, Shohei Yamashita, Yuji Masubuchi, Takashi Takeda and Shinichi Kikkawa

Page 2236

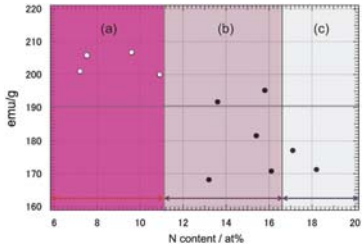

Humidity should be as low as possible to obtain a fine powder with a high α''-$Fe_{16}N_2$ content. An enhancement of magnetization to 210 emu g^{-1} at room temperature was observed from a nitrided mixture of α''-$Fe_{16}N_2$ with residual α-Fe, compared to 199 emu g^{-1} for an α-Fe fine powder reduced from γ-Fe_2O_3.

Nonstoichiometry of $ZnGeP_2$ crystals probed by static tensimetric method

I.G. Vasilyeva, R.E. Nikolaev and G.A. Verozubova

Page 2242

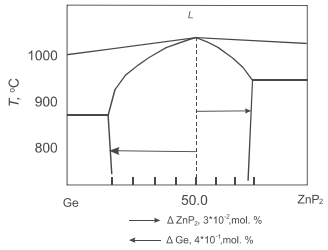

The nonstoichiometry of $ZnGeP_2$ on the T–x diagram of the ZnP_2–Ge system.

Structural and magnetic properties of self assembled Fe-doped Cu_2O nanorods

Asar Ahmed, Namdeo S. Gajbhiye and S. Kurian

Page 2248

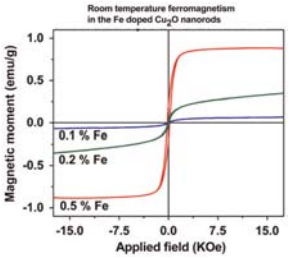

Ferromagnetism at room temperature was observed in the Fe doped Cu_2O nanorods. The origin seems to be the defects of cation vacancies created by the dopant ions.